www.MaterialsViews.com

Polycatechol Nanoparticle MRI Contrast Agents

*Yiwen Li, Yuran Huang, Zhao Wang, Fabio Carniato, Yijun Xie, Joseph P. Patterson, Matthew P. Thompson, Christopher M. Andolina, Treffly B. Ditri, Jill E. Millstone, Joshua S. Figueroa, Jeffrey D. Rinehart, Miriam Scadeng, Mauro Botta, and Nathan C. Gianneschi**

***A**mphiphilic triblock copolymers containing Fe^{III}-catecholate complexes formulated as spherical- or cylindrical-shaped micellar nanoparticles (**SMN** and **CMN**, respectively) are described as new T_1-weighted agents with high relaxivity, low cytotoxicity, and long-term stability in biological fluids. Relaxivities of both **SMN** and **CMN** exceed those of established gadolinium chelates across a wide range of magnetic field strengths. Interestingly, shape-dependent behavior is observed in terms of the particles' interactions with HeLa cells, with **CMN** exhibiting enhanced uptake and contrast via magnetic resonance imaging (MRI) compared with **SMN**. These results suggest that control over soft nanoparticle shape will provide an avenue for optimization of particle-based contrast agents as biodiagnostics. The polycatechol nanoparticles are proposed as suitable for preclinical investigations into their viability as gadolinium-free, safe, and effective imaging agents for MRI contrast enhancement.*

Dr. Y. Li, Z. Wang, Dr. J. P. Patterson,
Dr. M. P. Thompson, Dr. T. B. Ditri, Prof. J. S. Figueroa,
Prof. J. D. Rinehart, Prof. N. C. Gianneschi
Department of Chemistry and Biochemistry
University of California
San Diego, 9500 Gilman Dr., La Jolla, CA 92093, USA
E-mail: ngianneschi@ucsd.edu

Y. Huang, Y. Xie
Department of Materials Science and Engineering
University of California
San Diego, 9500 Gilman Dr., La Jolla, CA 92093, USA

Prof. F. Carniato, Prof. M. Botta
Dipartimento di Scienze e Innovazione Tecnologica
Università del Piemonte Orientale "A. Avogadro"
Alessandria, Italy

Dr. C. M. Andolina, Prof. J. E. Millstone
Department of Chemistry
University of Pittsburgh
4200 Fifth Ave., Pittsburgh, PA 15260, USA

Prof. M. Scadeng
Department of Radiology
University of California
San Diego, 9500 Gilman Dr., La Jolla, CA 92093, USA

DOI: 10.1002/smll.201502754

1. Introduction

Magnetic resonance imaging (MRI) is a frequently used radiological imaging modality that has become increasingly important in the diagnosis of human disease.[1] It is noninvasive and versatile, does not use ionizing radiation, and can be acquired at high resolution for obtaining anatomical and functional information on soft tissues.[2] However, the low sensitivity inherent to MRI has led to the development of MRI contrast agents that increase sensitivity by catalytically shortening the transverse (T_1) and longitudinal (T_2) relaxation times of water protons. Contrast agents belong to two categories defined by those that enhance contrast in a T_1- or T_2-weighted MRI experiment. Whereas most T_2-agents are represented by ferromagnetic inorganic nanoparticles,[3] the majority of T_1-agents consist of small molecule paramagnetic complexes.[4] Among T_1-agents, Gd^{III} contrast agents are most widely used in clinical MRI due to their high relaxivities ($1/T_1$), a manifestation of the short water residence times, long spin relaxation times, and seven unpaired electrons fostered by Gd^{III} ions.[4] Nonetheless, concerns have arisen regarding the release and accumulation of toxic Gd ions in vivo. For example, it has been reported that the administration

of Gd-based contrast agents to patients with renal dysfunction may induce the severe disease, nephrogenic systemic fibrosis.[5] An attractive nontoxic alternative to Gd-based, T_1-agents are those that feature high-spin d^5 Fe^{III} metal centers which have been shown to have significantly higher relaxivity than many other ions including Cu^{II}.[6] In addition, iron-based contrast agents remain appealing as various small molecule Fe^{III} complexes exhibit high biocompatibility and stability under physiological conditions.[7] Indeed, a number of iron chelates are proven therapeutics for the treatment of iron overload disease[8] and cancer.[9] In short, it is clear that, although effective, Gd-agents suffer from toxicity spurring a resurgence of interest in Gd-free MRI agents. Toward this goal, we have endeavored to explore nanoscopic materials incorporating multiple Fe^{III}-based chelates as T_1-weighted MRI contrast agents with high efficiency and inherently low toxicity.

The strong coordination bonds between Fe^{III} and catecholic ligands have been utilized extensively by natural systems in a variety of functional small molecules and biomaterials.[10] For example, the high iron affinity observed for the siderophore entorbactin is provided by a *tris*-catecholate ligand architecture.[11] Similarly, the mussel byssal cuticle employs 3,4-dihydroxy-L-phenylalanine (DOPA)-Fe^{III} complexes to provide strong, yet reversible crosslinking points, resulting in self-healing properties.[12] Interestingly, while small molecule iron^{III}*tris*-catecholate (Fe^{III}(catecholate)$_3$) complexes have been thoroughly explored as synthetic enterobactin mimics for iron sequestration, their potential to function as T_1-weighted MRI contrast agents has been largely overlooked despite their modest relaxivities.[13] Whereas marked improvements in the relaxivity and targeting specificity for Gd-based contrast agents has been achieved through the incorporation of small molecule Gd-chelates into nanomaterial scaffolds,[14] similar advances with Fe^{III}(catecholate)$_3$-based materials is in its infancy. Although synthetic catechol-based polymers with Fe^{III} have been widely described for a range of applications,[10,15] very limited examples have been explored as T_1-weighted MRI contrast agents. Indeed, the only system that has been studied are natural sepia melanins[16] and synthetic melanin-based materials in the form of polydopamines generated by oxidative polymerization.[17] Considering the many promising properties offered by poly(Fe^{III}-catecholate) materials, including high stability, low toxicity, and improved relaxivity, we considered it timely to prepare nanostructures consisting of polycatechol for the development of new MRI contrast agents.

Current strategies for the construction of poly(Fe^{III}-catecholate) as efficient T_1-weighted imaging agents for MRI generally focus on the complexation of natural sepia melanin colloidal particles with Fe^{III} salts.[16,17] However, the development of functional and robust contrast agents from melanin-type materials has been met with profound challenges. Issues include limited control over the synthetic colloidal chemistry hindering size and shape control over the resulting melanin particles.[15a] We believe that more sophisticated strategies making use of self-assembled soft materials from amphiphilic block copolymers,[18] with the integration of Fe^{III}-catecholate blocks, may provide an avenue for preparing particles of well-defined and predictable morphologies. Certainly, these are undoubtedly critical, and highly desirable properties if one aims to prepare materials for in vivo use.[19] This would be enabled by the use of a controlled living polymerization method, giving rise to well-defined and reproducibly accessible block copolymer architectures. We propose that the resulting supramolecular nanostructures from such copolymers with rigorously controlled physical parameters (i.e., size, shape, and composition) would represent a new class of macromolecular Gd-free T_1-weighted MRI contrast agent. Control over these parameters is a must as it is widely known that the fundamental physical properties of nanoparticles may affect their behavior within biological systems.[20] In this work, we report our first effort toward this goal through the design and synthesis of polycatechol-based amphiphilic block copolymers and the elucidation of the relaxation properties of the resulting self-assembled micellar nanoparticles.

2. Results and Discussion

2.1. Molecular Design and Micellar Nanoparticle Formation

Our synthetic approach employed post-polymerization functionalization[18c,d] for the incorporation of multiple catechol groups localized in the middle block of a triblock copolymer amphiphile (**Figure 1**). The macromolecular precursors, $(OEG)_m$-$(NHS)_n$-$(C_6)_p$, were directly synthesized via ring-opening metathesis polymerization (ROMP)[21] (Figures S1 and S2, Supporting Information) using a modified 2nd generation Grubbs' catalyst (Figure 1a). Excess dopamine hydrochloride was then added to the macromolecular precursors in the presence of *N*,*N*-diisopropylethylamine (DIPEA) to afford the final products. Notably, a post-polymerization functionalization route was taken when it was discovered that catechol-modified norbornene monomers would not polymerize utilizing this class of initiator for ROMP.[15e] Regardless, this synthetic approach achieved a near quantitative incorporation of catechol groups into the middle region of the block copolymers as determined by the ^{1}H NMR and ^{13}C NMR (Figures S3–S6, Supporting Information). Both of the resulting amphiphilic triblock copolymers (Polymers 1 and 2) are solids with limited solubility in nonpolar organic solvents. By varying the segment size of each block in the amphiphilic copolymers to tune the volume fraction of hydrophobic domain, two kinds of stable micellar morphologies (i.e., sphere and cylinder) could be obtained (Figure 1b–g).

The assembly of resulting catechol-based amphiphilic block copolymers was performed in a selective solvent to generate the two different micelles.[22] Specifically, to prepare a spherical micellar nanoparticle (**SMN**), an aqueous solution of $FeCl_3$ (1 mg mL^{-1}) was added at a rate of 10 μL h^{-1} to a vial containing 2 g of a stock solution of Polymer 1 in THF as a common solvent, with an initial concentration of 2.0 wt% until the final water content reached 70 wt%. The stable **SMN** were then obtained by dialyzing the micelle solution against deionized water for 3 d to remove the organic solvent and any unchelated Fe^{III} ion. Cylindrical micellar nanoparticles (**CMN**) were generated using Polymer 2 which consists of a

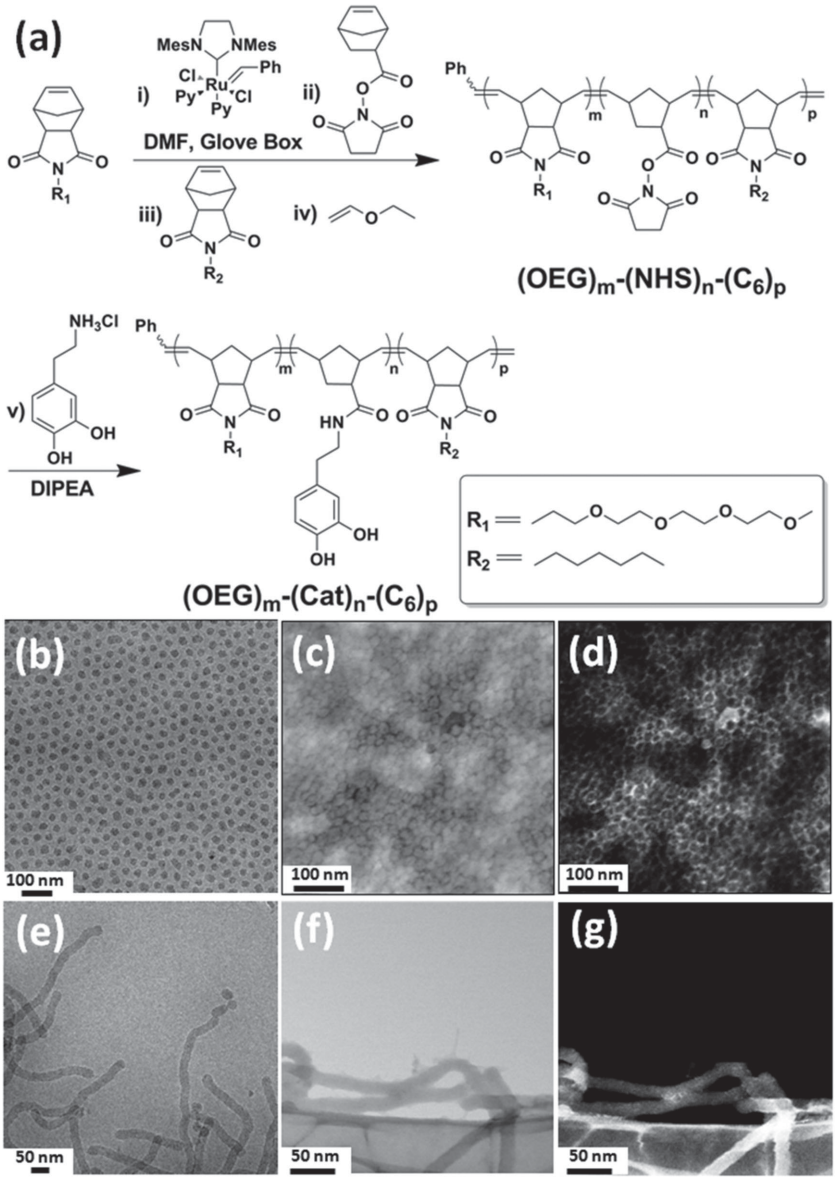

Figure 1. General synthetic scheme for amphiphilic triblock copolymers, and electron microscopy of the resulting micellar nanoparticles. a) Polymer 1: m = 38, n = 34, p = 50. Polymer 2: m = 20, n = 23, p = 43; b–d) Electron microscopy of **SMN** formed from Polymer 1: (b) cryo-TEM. (c) BF-STEM. (d) HAADF-STEM; e–g) Electron microscopy of **CMN** formed from Polymer 2: (e) cryo-TEM. (f) BF-STEM. (g) HAADF-STEM.

higher volume fraction of the hydrophobic domain, under precisely the same conditions.[22a]

Each of the two well-defined micellar morphologies were characterized by cryo-transmission electron microscopy (TEM) (Figure 1b,e) and dry state TEM (Figure S7, Supporting Information), demonstrating diameters for **SMN** and **CMN** of ≈30 and 25 nm, respectively. Although precise control over the micellar length of **CMN** is not possible,[23] it can be clearly observed that a majority of **CMN** possess long (>1 μm) cylindrical lengths. The presence of high contrast metal elements (heavy nuclei) in both **SMN** and **CMN** was evident in bright field scanning transmission electron microscopy (BF-STEM) (Figure 1c,f) and high angle annular dark field (HAADF)-STEM (Figure 1d,g). Moreover, selected area BF-STEM coupled with energy dispersive X-ray spectroscopy (EDS) confirmed the presence of metal ions localized inside the micellar nanoparticles (Figures S8 and S9, Supporting Information). Specifically, the EDS profiles suggested that the content of Fe in the testing areas of **SMN** and **CMN** were significantly higher than those on the grid surface background, which are in good agreement with the elemental mapping analysis results (Figures S8a and S9a, Supporting Information). Furthermore, TEM was used to confirm that both **SMN** and **CMN** are stable in aqueous solution for at least six months (Figure S10, Supporting Information).

2.2. Relaxometric Characterization of Micellar Nanoparticles

The basic relaxation properties of **SMN** and **CMN** were first investigated using their ^{1}H $1/T_1$ nuclear magnetic relaxation dispersion (NMRD) profiles acquired under magnetic field strengths from 0.01 to 70 MHz (**Figure 2**). Inductively coupled plasma-optical emission spectrometry (ICP-OES) was employed to calibrate the Fe concentration of **SMN** and **CMN** solutions. The NMRD profiles show a similar shape and different amplitude. In both cases there is a poorly defined plateau at low fields (≈0.01–0.05 MHz), followed by a wide dispersion (≈0.05–7 MHz) and by a broad hump at higher frequencies. The ratio of the relaxivity values at low (0.01 MHz) and high fields (60 MHz) amounts to 1.6 and 1.4 for **CMN** and **SMN**, respectively. Relaxivity, r_1, arises from metal-bound and/or proximate hydrogen-bonded water molecules, dipolarly interacting with the unpaired electrons of the metal ion

$$r_1 = f_M \times (T_{1M} + T_M)^{-1} + r_1^{os} \quad (1)$$

where f_M is the mole fraction of interacting water molecules, T_{1M} their proton relaxation time due to the paramagnetic Fe^{III} ion, τ_M the exchange lifetime, and r_1^{os} the contribution of outer-sphere fast diffusing water protons.[24] T_{1M} depends on r^6, the distance of the interacting dipoles, on the correlation time (τ_C) for the proton–electron dipolar interaction and on ω_I and ω_S, the proton and electron Larmor frequencies, respectively. The inflection point in the profiles reflects the condition $\omega_S\tau_C = 1$, so that we can estimate a value of ≈0.4–0.6 ns for the correlation time. The appearance in both profiles of broad humps at high fields with relaxivity values well above 6 $mM^{-1}s^{-1}$ represents a strong indication that the

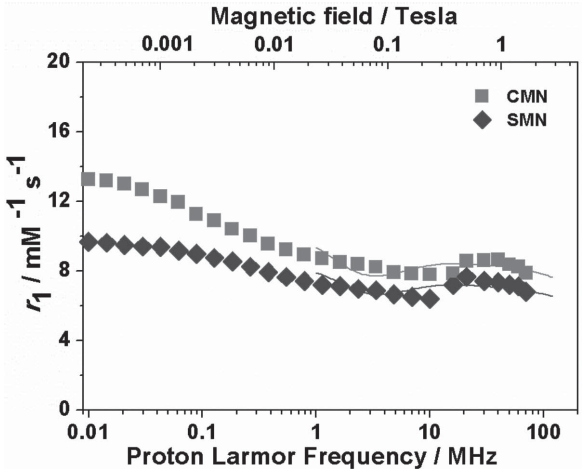

Figure 2. ^{1}H NMRD profiles for **SMN** and **CMN** at 298 K.

relaxivity is not dominated by a simple outer-sphere mechanism. Although this high relaxivity might originate from the presence of inner-sphere water interactions afforded by dynamic $Fe^{III}(catecholate)_2(H_2O)_2$ moieties, we speculate the enhanced relaxivity may largely originate from the presence of one or more second-sphere interactions to a coordinatively saturated, six-coordinate, $Fe^{III}(catecholate)_3$,[25] similar to those observed for small molecule $Fe^{III}(catecholate)_3$ complexes.[13] These second-sphere interactions likely take the form of dynamic hydrogen bonds between H_2O and polar groups on the nanoparticle proximal to $Fe^{III}(catecholate)_3$ sites, or to oxygen atoms of the $Fe^{III}(catecholate)_3$ sites themselves. Indeed, several structurally characterized $Fe^{III}(catecholate)_3$ complexes have been reported that feature hydrogen bonds between oxygen atoms of the FeO_6 core and polar H-X units (X = O, N) (see five examples from Cambridge Structural Database listed in Figures S11–S15, Supporting Information). Moreover, direct X-ray crystallographic evidence for hydrogen bonding between the hydrogen atoms of water and the oxygen atoms of a transition-metal catecholate has been observed in both Ni[26] and Mn[27] complexes, thereby suggesting that such second-sphere H_2O interaction modes are viable in these nanoparticle systems.

Therefore, based on this precedent, the data were fit to calculate rotational correlation times of 490 and 448 ps for **CMN** and **SMN**, respectively, assuming the presence of two second-sphere water molecules at a long-range distance of 3.3 ± 0.1 Å from the Fe center with a residence lifetime of ≈2 μs[28] (**Table 1**, details of the best-fit parameters can be found in the Supporting Information). These results are in good agreement with similar findings reported for bovine lactoferrin[28] and methemoglobin.[29] In addition, both **SMN** and **CMN** exhibit substantially higher r_1 than that of mononuclear $Fe^{III}(catecholate)_3$ complexes (e.g., at a field of 20 MHz, r_1 values for **SMN** and **CMN** are 8.0×10^{-3} and 9.0×10^{-3} M^{-1} s^{-1}, respectively, while r_1 for small molecule $Fe^{III}(catecholate)_3$ complexes are $\approx 2.0 \times 10^{-3}$ M^{-1} s^{-1}),[13c] indicating that the macromolecular scaffolds effectively increase the relaxivity of contrast agent moieties by restricting the rotational mobility of the complex (i.e., of the vector connecting Fe^{III} and the protons of second sphere water molecules).[30] Moreover, the per Fe^{III} r_1 of **SMN** and **CMN** outperforms clinically used Gd^{III} contrast agents across a wide range of applied magnetic field strengths (>10 MHz) (see the Supporting Information). For example, measured enhancements over Gd-DOTA are +100% and +69% for **CMN** and **SMN**, respectively, at 1.0 T and 298 K (Figure S16, Supporting Information).

It should be noted that NMRD profiles are fitted herein only in the high field region because of the known limitations of Solomon–Bloembergen–Morgan (SBM) theory in the slowly rotating regime that render it unable to completely account for the behavior of slowly rotating systems at very low magnetic field strengths, where the Zeeman energy is smaller than the zero field splitting energy.[31] In addition, it is worth mentioning that the deviation of the profiles from the behavior of a well-defined Lorentzian might be compatible with the presence of different, nonequivalent Fe^{III} ions in the nanoparticles.[13b] The NMRD profiles may reflect different structures and dynamics (number, distance, and lifetime) of second sphere water molecules around the Fe centers, which have characteristic and different electronic relaxation times.[3b]

The longitudinal and transverse relaxation times (T_1 and T_2) of both nanoparticles, with various concentrations, at clinically relevant field strengths (B_o = 1.41 T) were measured using time-domain NMR to quantitatively calculate their relaxivity values (r_1 and r_2) (**Figure 3** and Figure S17, Supporting Information). Both **SMN** and **CMN** exhibit high relaxivity values ($r_{1,\mathbf{SMN}} = 7.1 \times 10^{-3}$ M^{-1} s^{-1}, $r_{1,\mathbf{CMN}} = 7.9 \times 10^{-3}$ M^{-1} s^{-1}) for potential clinical use (based on the calculated results shown in Figure 3a,b, Figure S17, Supporting Information, and **Table 2**).[17a] In summary, the excellent contrast enhancement of the Fe^{III}-chelated micellar nanoparticles was mainly attributed to second-sphere contributions, as discussed above. Moreover, the low r_2/r_1 ratios of both **SMN** and **CMN** (r_2/r_1 = 1.25 for **SMN**, and r_2/r_1 = 1.40 for **CMN**) favor positive contrast enhancement (brightening) because the interference from T_2 effects (darkening) are relatively small. Overall, the high T_1 relaxivity and low r_2/r_1 ratio of both micellar nanoparticles could make them suitable as Gd-free clinical contrast agents for T_1-weighted MRI. This conclusion is supported by the bright T_1-weighted MR images from **SMN** and **CMN** in aqueous solution (Figure 3c).

Variable field and temperature magnetic measurements were performed using a superconducting quantum interference device (SQUID) to confirm that

Table 1. Selected relaxation parameters obtained from the analysis of NMRD profiles shown in Figure 2.

Micelles	$^{20}r_1$[a] [$\times 10^{-3}$ M^{-1} s^{-1}]	Δ^2[b] [10^{19} s^{-2}]	τ_V[b] [ps]	τ_R [ps]	R [Å]	q[c]	τ_M [μs]
SMN	7.7	1.4 ± 0.1	54 ± 3	448 ± 8	3.3 ± 0.1	2	2.0 ± 0.1
CMN	8.6	1.1 ± 0.2	50 ± 4	490 ± 12	3.3 ± 0.1	2	1.9 ± 0.2

[a]20 MHz and 298 K; [b]The parameters for electronic relaxation are used as empirical fitting parameters and do not have a real physical meaning for slowly tumbling nanosized systems. Low-field data, those most affected by electronic relaxation, were not included in data analysis; [c]Fixed during the fit.

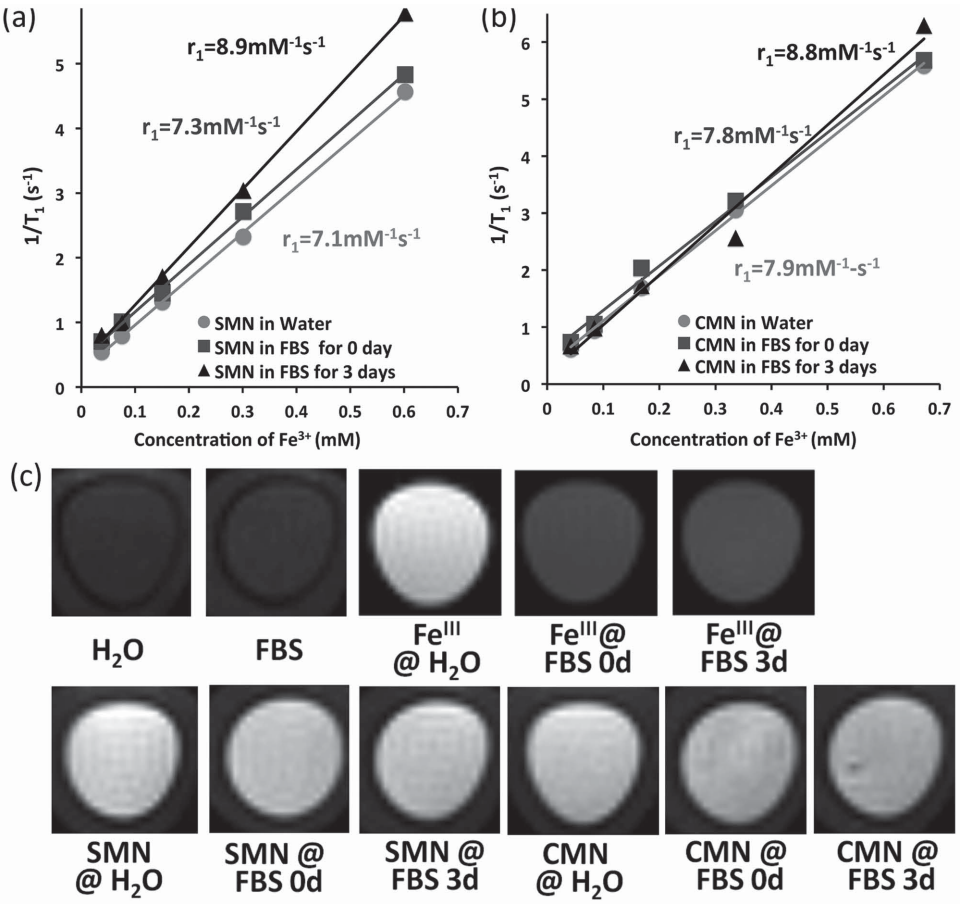

Figure 3. MRI characterization of micellar nanoparticles. a) Plots of $1/T_1$ versus Fe^{III} concentration for **SMN** in different medium with calculated r_1 (blue plot: **SMN** in water, red plot: **SMN** in freshly prepared FBS, and green plot: **SMN** in FBS for 3 d); b) Plots of $1/T_1$ versus Fe^{III} concentration for **CMN** in different medium with calculated r_1 (blue plot: **CMN** in water, red plot: **CMN** in freshly prepared FBS, and green plot: **CMN** in FBS for 3 d); c) T_1-weighted MR images captured on a Bruker 7.0 T magnet from free Fe^{III}, **SMN** and **CMN** in different media ([Fe^{III}] is at 0.6×10^{-3} M in each tube).

the observed MRI contrast arises from multiple isolated Fe^{III}-catecholate sites. Plots of magnetization versus applied magnetic field show significant curvature only at temperatures less than 24 K, consistent with isolated paramagnetic iron centers (**Figure 4**). The lack of magnetic saturation, even at 7 T and 2 K, indicates a significant magnetic anisotropy associated with the spin state and coordination environment of the Fe^{III}; however, quantitative fitting of the data was not possible. This indicates that a range of Fe^{III} environments may be present within **SMN** and **CMN** micelles, as suggested by the broad NMRD profiles. At temperatures exceeding 24 K, the magnetization is completely linear with the applied field, confirming that the MRI contrast ability of **SMN** and **CMN** results from many isolated Fe^{III}-catecholate complexes inside the micellar nanoparticles.

Table 2. Relaxivity data for micellar nanoparticles in different media. (The magnetic field strength for T_1 and T_2 measurement is 1.41 T.)

Micelles	Media	r_1 [$\times 10^{-3}$ M^{-1} s^{-1}]	r_2 [$\times 10^{-3}$ M^{-1} s^{-1}]	r_2/r_1
SMN	H_2O	7.1	8.9	1.25
CMN	H_2O	7.9	11.1	1.40
SMN	FBS (fresh)	7.3	10.2	1.40
CMN	FBS (fresh)	7.8	10.6	1.36
SMN	FBS (3 d)	8.9	10.4	1.17
CMN	FBS (3 d)	8.8	13.3	1.51

2.3. Long-Term Stability of Micellar Nanoparticles

The stability of **SMN** and **CMN** in serum was also examined in two respects: (1) No collapse or change of the micellar nanoparticle morphologies was observed over time; (2) The total metal ion content and relaxivity values of the Fe^{III}-chelated nanoparticles does not change significantly over time. With regards to morphological stability, we propose that although many previously established micelle-based therapeutic systems have suffered from an inherent instability in vivo (generally undergoing collapse or break-up in the presence of serum lipids and proteins),[32] the micellar particles described here benefit from cross-linking networks of individual polymer chains in the micellar interface via the

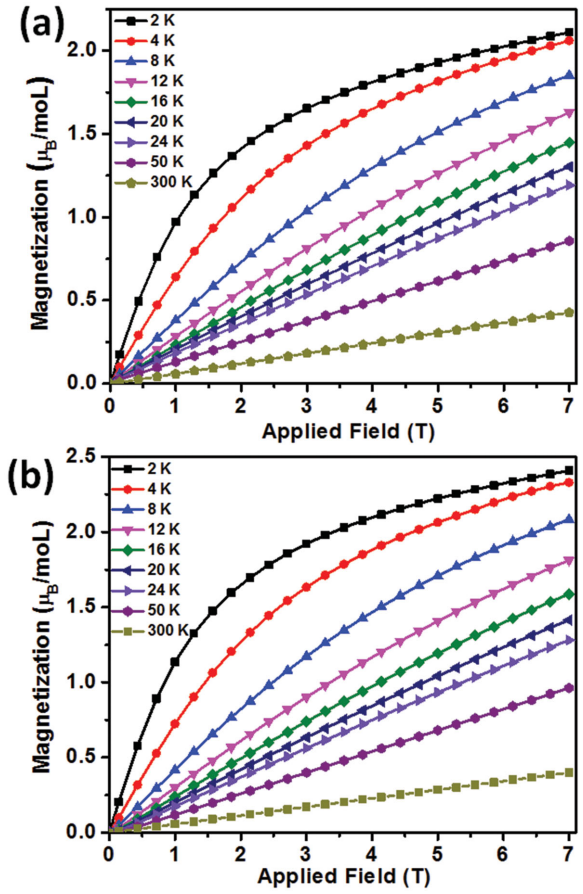

Figure 4. Magnetization data collected as a function of applied field for a) **SMN** and b) **CMN** from 2 to 300 K.

formation of interchain, multiple Fe^{III}-catecholate coordination bonds.[12,33] These crosslinks lead to the particles being stable for more than 20 d in fetal bovine serum (FBS, 100%) even at a high concentration (>20 mg mL^{-1}). With regards to the strong binding capacity and affinity of catechols for Fe^{III},[10] we performed a stability assay of Fe^{III}-chelated **SMN** and **CMN** in PBS solution to show that there was no iron release from micellar nanoparticles at different incubation time points (Figure S18, Supporting Information). It can be clearly seen that the metal ion content of **SMN** and **CMN** in PBS are ≈100% after 7 d. Accordingly, the r_1 and r_2 values of both **SMN** and **CMN** after 3 d incubation in FBS are almost identical to the ones corresponding to freshly prepared micellar nanoparticles (Figure 3a,b, Figure S17, Supporting Information, and Table 2), which is in good agreement with that observed in T_1-weighted MR images (Figure 3c). The very slight increase in relaxivity values of **SMN** and **CMN** might be due to interactions between nanoparticles and proteins in FBS.[34] The intensity of bright MR images for several **SMN** and **CMN** samples in different media with various incubation times is also found to be very similar. However, the MRI signal from free Fe^{III} was observed to be immediately quenched in FBS (Figure 3c), likely due to the participation of free ions in redox reactions in the biological fluid.[35] This result also suggests that metal ions were not leaking from the nanoparticles after the 3 day incubation in serum, as the MR images do not lose intensity over that time frame (Figure 3c). We conclude that the materials exhibit promising stabilities in biological media.

2.4. Shape-Dependent MR Imaging of Micellar Nanoparticles in HeLa Cells

Prior to investigating the MR imaging performance of the micellar nanoparticles in HeLa cells, their cytotoxicity at various concentrations of Fe^{III} was assessed using a CCK-8 (cell counting kit-8) assay. Similar to Fe^{III}-chelated melanin colloidal nanoparticles[17a] and many other kinds of polycatechol-based biomaterials,[15a,36] both **SMN** and **CMN** also show high biocompatibility and promisingly low toxicity with respect to live cells. Cell viability was measured in HeLa cells using micellar nanoparticles with various dosages from 0.5 to 100 × 10^{-6} M Fe^{III} for 24 and 48 h incubation. Under these conditions, cell viability was maintained at ≈100% in all groups (Figure S19, Supporting Information).

Next, **SMN** and **CMN**, with identical [Fe^{III}] concentrations (67.5 × 10^{-6} M), were incubated with HeLa cells for different periods of time. Quantitative analysis of cellular iron uptake and the corresponding T_1 relaxation values were measured by ICP-OES and MRI, respectively (**Figure 5**). HeLa cells incubated with **SMN** and **CMN** exhibited enhanced positive contrast in T_1-weighted MR images compared with control cells (incubation times: 24 or 48 h) (Figure 5a). Surprisingly, it was found that T_1-weighted MR images of HeLa cell pellets incubated with **CMN** exhibited much stronger T_1 signal enhancement (shorter T_1 relaxation time) compared with those incubated with **SMN** after short incubation times (4 or 12 h) (Figure 5a). Quantitative analysis of intracellular iron indicated cell uptake (Figure 5b,c) was indeed shape- and time-dependent (Figure 5d). For **CMN**, cell uptake significantly increased in the first 4 h, then slowed, reaching a plateau at 12 h, which is in good agreement with the T_1 values of each corresponding cell pellet. By contrast the intracellular Fe^{III} content of **SMN** gradually increased without saturation over a period of 48 h (Figure 5d), matching the decreasein T_1 values of the cell pellets over the incubation time. Additionally, MR imaging of **CMN**-treated HeLa cells exhibits brighter positive contrast and shorter relaxation times than **SMN**-treated cells at identical initial [Fe^{III}] concentrations and incubation times, particularly when short incubation times (i.e., 4 h) were employed.

In terms of mechanism, it is possible that these differences are explained by the fact that **CMN** is capable of making multiple contacts with the cell surface providing an initially stronger association leading to faster and more efficient uptake. Indeed, in this context it is important to note that various observations have been made concerning shape-dependent polymeric nanoparticle cell internalizati on.[20b,37] However, general trends and mechanisms are yet to be elucidated, as uptake efficiencies vary by nanoparticle composition, flexibility, surface charge, overall dimensions and aspect ratio, and other confounding factors.[20b,37,38] In this study, poly(Fe^{III}-catecholate)-based nanoparticles were internalized into HeLa cells to a higher extent when they

www.MaterialsViews.com

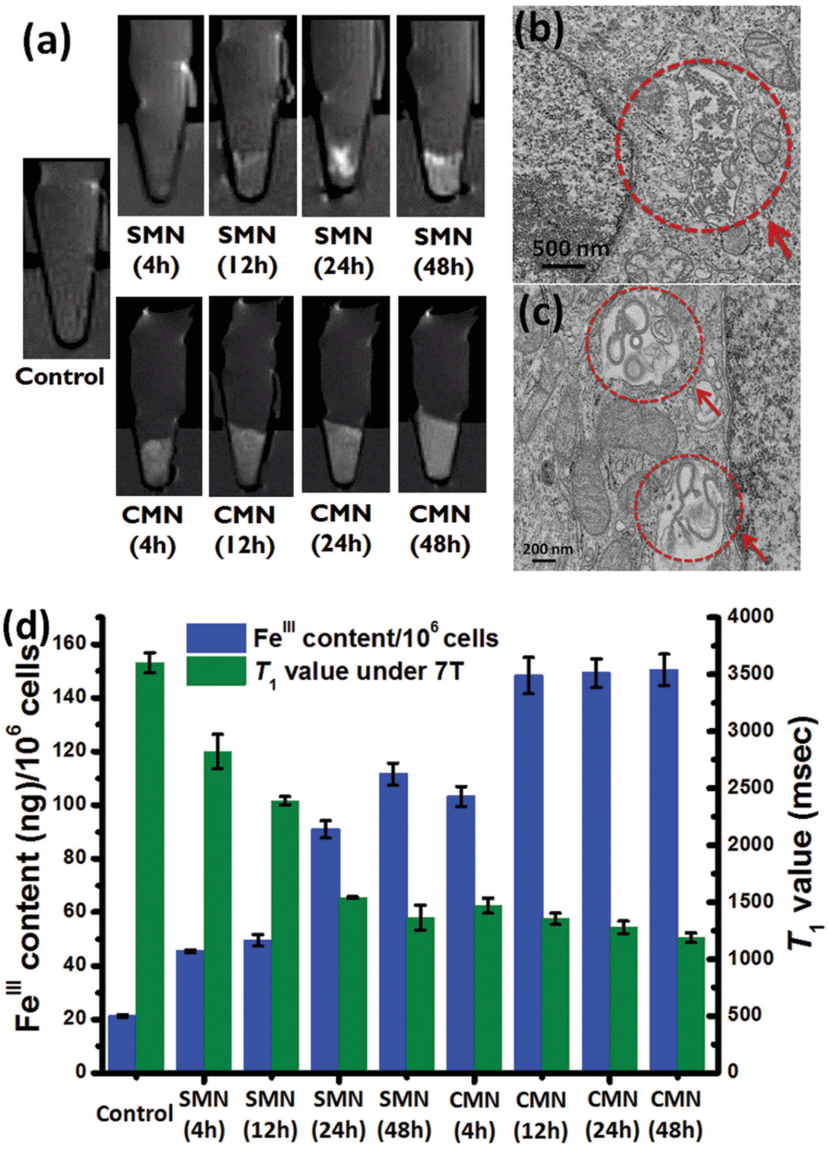

Figure 5. a) In vitro T_1-weighted MR images of HeLa cells incubated with **SMN** and **CMN** ([Fe^{III}] is 67.5×10^{-6} M) for different periods of time; TEM image of b) **SMN** and c) **CMN**, trapped inside vesicles of HeLa cells (see Figure S20 of the Supporting Information for additional cellular TEM images); d) Quantitative determination of intracellular Fe^{III} content (per 10^6 cells) for HeLa cells incubated with **SMN** and **CMN** for different periods of time and their corresponding T_1 relaxation values.

were of a cylindrical morphology than when they were in the form of spherical particles (Figure 5b,c). A similar trend was also reported for shell-crosslinked spherical and cylindrical micelles,[39] as well as polymer brush-based spherical and long rod-like nanostructures.[38] Considering that shape not only plays an important role in cell internalization, but can also be a determining factor in overall biodistribution patterns in vivo (i.e., blood circulation and extravasation),[20a,38] these preliminary results introduce exciting opportunities for optimization and tunability in the design of self-assembled nanoparticles. This highlights the power of the approach for the preparation of nanoparticles from well-defined polymers generated utilizing a living polymerization. Indeed, as a demonstration of this concept, the approach taken here provides direct access to two well-defined morphologies of polycatechol-based nanoparticle, not easily achievable utilizing analogous synthetic melanin colloidal nanoparticles prepared by oxidative polymerization.

3. Conclusion

In summary, we have developed a new class of efficient and biocompatible MRI contrast agents based on micellar nanoparticles formed from amphiphilic poly(Fe^{III}-catecholate)-based copolymers. Compared with recently reported natural or synthetic melanin-based T_1 agents, our approach utilizes well-defined triblock copolymers prepared via a controlled living polymerization method. This synthetic route gives access to a tunable polymer system and hence, differently shaped self-assembled nanoparticles with controlled physical parameters. These nanoparticles have the potential to be used for various applications in diagnostic radiology and imaging, due to their enhanced relaxivity, and long-term stability in biological media. Moreover, we further demonstrate that the resulting nanoparticles provide enhanced positive contrast for MR imaging in HeLa cells. Notably, we observed shape-dependent behavior in terms of cellular uptake with cylindrical micelles exhibiting brighter contrast and shorter relaxation times than the analogous spherical micelles. We present this study with the goal that it stimulates further investigation of polycatechol nanoparticles in terms of their potential as Gd-free MRI contrast agents. Work in our own laboratory on shape-dependent behavior in vivo is underway with respect to both intraperitoneal and intravenous delivery of polycatechol nanoparticle-based contrast agents.

4. Experimental Section

Monomer and Polymer Synthesis and Characterization: All chemicals were purchased from commercial sources and used without further purification, unless otherwise indicated. Anhydrous toluene and dichloromethane were purified using a Dow-Grubbs two-column purification system (Glasscontour System, Irvine, CA).[40] $(IMesH_2)(C_5H_5N)_2(Cl)_2Ru$ = CHPh was prepared as described by Sanford et al.[41] Monomers **1, 2, 3** were synthesized as previously reported.[18a,42] Polymerizations were performed under a dry dinitrogen atmosphere with anhydrous, degassed solvents in a glove box.

^1H (400 MHz) and ^{13}C (100 MHz) NMR spectra were recorded on a Varian Mercury Plus spectrometer. Chemical shifts (^1H) are

reported in δ (ppm) relative to the C_5D_5N residual proton peaks (δ 7.22, δ 7.58, and δ 8.74 ppm). Chemical shifts (^{13}C) are reported in δ (ppm) relative to the C_5D_5N carbon peaks (δ 123.87, δ 135.91, and δ 150.35 ppm). All ^{13}C NMR spectra were proton decoupled. Mass spectra were obtained at the UCSD Chemistry and Biochemistry Molecular Mass Spectrometry Facility. Polymer dispersities and molecular weights were determined by size-exclusion chromatography (Phenomenex Phenogel 5 μ 10, 1 K-75 K, 300 × 7.80 mm in series with a Phenomex Phenogel 5 μ 10, 10 K-1000 K, 300 × 7.80 mm (0.05 M LiBr in DMF) using a Shimatzu pump equipped with a multiangle light scattering detector (DAWN-HELIOS: Wyatt Technology) and a refractive index detector (Optilab T-rEX: Wyatt Technology) normalized to a 30 000 MW polystyrene standard using dn/dc of 0.100 for all the polymers.

Micelles Preparation and Characterization: The samples were first dissolved in THF as the common solvent and stirred at room temperature overnight to ensure complete dissolution of the polymer to prepare a stock solution with an initial concentration of 2 wt%. The solution was then filtered through a filter of 0.22 μm pore size to remove any dust. $FeCl_3$ solution (1 mg mL^{-1}) was filtered through a filter of 0.22 μm pore size and added dropwise at a rate of 10 μL h^{-1} using a syringe pump into a vial containing 2.00 g of the stock solution. $FeCl_3$ solution addition was continued until reaching a final water content of 70 (wt)%. Then the micelle solution was dialyzed against deionized water for 3 d to remove the common solvent, excess Fe^{III} and fix the micellar morphology.

Snakeskin dialysis tubing was purchased from Thermoscientific, Inc. with a molecular weight cut off (MWCO) of 10 000 g mol^{-1}. TEM was performed on a FEI Sphera microscope operating at 200 keV. TEM grids were prepared by depositing small (3.5 μL) aliquots of sample onto grids (≈2 min, Formvar stabilized with carbon (5–10 nm) on 400 copper mesh, Ted Pella Inc.) that had previously been glow discharged using an Emitech K350 glow discharge unit and plasma-cleaned for 90 s in an E.A. Fischione 1020 unit. Images were recorded on a 2 K X 2 K Gatan CCD camera.

Cryo-TEM experiments were also performed on a FEI Sphera microscope operating at 200 keV. TEM grids were prepared by depositing small (3.5 μL) aliquots of sample onto grids (Quantifoil R2/2 holey carbon) that had previously been glow discharged using an Emitech K350 glow discharge unit and plasma-cleaned for 90 s in an E.A. Fischione 1020 unit. Sample was loaded onto the grids at 4 °C, blotted with filter paper to create a thin film on the grid, then plunged into liquid ethane and transferred into a precooled Gatan 626 cryo-transfer holder, which maintained the specimen at liquid-nitrogen temperature in a FEI Sphera microscope operated at 200 keV. Images were recorded on a 2 × 2 K Gatan CCD camera.

STEM and STEM-EDS analysis were acquired on a JEOL JEM 2100F TEM equipped with an INCA (Oxford) EDS detector at the NanoScale Fabrication and Characterization Facility (NFCF), Peterson Institute of Nanoscience and Engineering (PINSE), University of Pittsburgh, PA. Samples were prepared by drop-casting 5 μL of sample onto TEM grids (ultrathin 5 nm A-type carbon with 400 mesh copper, Ted Pella, Inc.) followed by slow drying covered on the bench top for at least 3 h. Samples were then dried under vacuum for 24–48 h to remove contamination that would interfere with STEM-EDS. Grids were loaded into a JEOL 31640 beryllium double tilt holder. STEM-EDS data were collected for 180–600 s at specific points, using the largest probe size (1.5 nm electron beam diameter) with a 200 kV accelerating voltage. Images were collected in bright field (BF) and high-angle annular dark field (HAADF) modes.

The magnetic properties of micellar nanoparticles were characterized using a Quantum Design MPMS3 superconducting quantum interference device (SQUID) with a maximum field of 7 T. Freeze-drying solid samples (≈10 mg) were packed into standard Quantum Design plastic sample holders. Magnetization data were collected in DC mode and corrected for diamagnetic contributions using Pascal's constants.

Fe^{III} Concentration Determination in Micelles: In order to determine Fe^{III} concentration, the metal was first stripped from the polymers using the following procedure. To an aliquot of each sample (100 μL) was added 1% HNO_3 in water (1900 μL). Each mixture was then stirring for about 12 h. Then the Fe^{III} concentration was quantified by inductively coupled plasma-optical emission spectrometry (ICP-OES) using a Perkin Elmer Optima 3000DV spectrometer in the Scripps Institution of Oceanography, University of California, San Diego.

Fe^{III} Stability in PBS: To determine the stability of Fe^{III} chelated in **SMN** and **CMN**, we redispersed these two types of micellar nanoparticles in PBS (pH = 7.4). 300 μL of SMN and CMN solution (three replicates) were added in 500 μL dialysis tubes with M_w = 3500, respectively, and dialyzed to 500 mL PBS (pH = 7.4) under room temperature with magnetic stirring. 20 μL **SMN** and **CMN** aliquots were taken at time points as 8 h, 24 h, 48 h, 72 h, 7 d for ICP-OES analysis.

Determination of the In Vitro Stability of Micelles in FBS by MRI Analysis: Samples of both **SMN** and **CMN** were prepared in FBS at various [Fe^{III}] concentrations (For **SMN**, 5 [Fe^{III}] concentrations were used: 0.6×10^{-3} M, 0.3×10^{-3}, 0.15×10^{-3}, 0.075×10^{-3}, and 0.038×10^{-3} M; while for **CMN**, 5 [Fe^{III}] concentrations were used: 0.67×10^{-3}, 0.34×10^{-3}, 0.17×10^{-3}, 0.08×10^{-3}, and 0.04×10^{-3} M) 3 d prior to MRI analysis, and as controls, samples of identical concentration to the latter were prepared in both FBS and water immediately before MRI analysis (named, **SMN**/**CMN** in FBS for 3 d, **SMN**/**CMN** in freshly prepraed FBS, and **SMN**/**CMN** in water, respectively). Longitudinal and transverse relaxation time (T_1 and T_2) measurements were acquired with a Bruker Minispec mq60 (1.41 T or 60 MHz, 37 °C). Relaxivities (r_1 and r_2) were calculated by linearly fitting plots of $1/T_1$ (s^{-1}) or $1/T_2$ (s^{-1}) versus Fe^{III} ions concentrations (μM). MR images were acquired on a Bruker 7.0 T magnet equipped with Avance II hardware and a 72 mm quadrature transmit/receive coil ([Fe^{III}] = 0.6 mM in each tube). T_1 contrast was determined by selecting regions of interest (ROI) using the ParaVision Version 5.1 software. The fitting parameters for 7 T MRI analysis are as follows: TR = 750.0 ms, TE = 12.6 ms, echo = 1/1, FOV = 6.91/3.12 cm, slice thickness = 2 mm, nex = 2 mm, matrix = 256*116.

^1H NMRD Profiles: Proton $1/T_1$ NMRD profiles were measured on a fast field-cycling Stelar SMARTracer Relaxometer (Stelar, Mede (PV), Italy) at magnetic field strengths from 0.00024 to 0.25 T (corresponding to 0.01–10 MHz proton Larmor frequencies) at room temperature. The relaxometer operates under computer control with an absolute uncertainty in $1/T_1$ of ±1%. Additional data points in the range 15–70 MHz were obtained on a Bruker WP80 NMR electromagnet adapted to variable-field measurements (15–80 MHz proton Larmor frequency) Stelar Relaxometer. The ^1H T_1 relaxation times were acquired by the standard inversion

recovery method with typical 90° pulse width of 3.5 μs, 16 experiments of 4 scans. The temperature was controlled with a Stelar VTC-91 airflow heater equipped with a calibrated copper-constantan thermocouple (uncertainty of ± 0.1 °C).

Cell Viability: In vitro cytotoxicity of micellar nanoparticles was determined in HeLa cells by the CCK-8 (cell counting kit-8) assay. HeLa cells were incubated on 96-well plates with 1×10^4 cells per well in High-glucose DMEM medium containing 10% fetal bovine serum and 1% antibiotics at 37 °C in 5% CO_2 humidified atmosphere for 24 and 48 h respectively. Addition of 10 μL of CCK-8 solution to each well and incubation for another 4 h at 37 °C resulted in the formation of formazan crystals. Then the absorbance value at 460 nm was recorded using a microplate reader. The absorbance value of the untreated cells was used as the reference value of 100% cellular viability.

Shape- and Time-Dependent MR Imaging in HeLa cells: HeLa cells were seeded in 15 cm round tissue culture dishes and allowed to attach overnight. After washing twice with sterile PBS, the cells were incubated with micellar nanoparticles (the concentration of Fe^{III} ions was $\approx 67.5 \times 10^{-6}$ M) for different times including 4, 12, 24, and 48 h, respectively, at normal cell culture condition. The cells were washed with PBS three times in order to remove excess nanoparticles, and then treated with 0.05% trypsin to remove them from the dishes. The cells were gathered by centrifuge at 300 g for 3 min and washed with PBS buffer twice. The number of cells in each sample was counted for further use. The cell MR images were acquired on a Bruker 7.0 T magnet with Avance II hardware equipped with a 72 mm quadrature transmit/receive coil. T_1 contrast was determined by selecting regions of interest (ROI) using Software ParaVision Version 5.1. The parameters for 7 T MRI are: TR = 1000.0 ms, TE = 12.6 ms, echo length = 1, FOV = 7.91/3.22 cm, slice thickness = 1 mm, nex = 1 mm, matrix = 256*104. Then, the cells were digested by 70% HNO_3 solution under bath sonication for overnight, in order to test the iron ions content by ICP-MS. The Fe^{III} quantities of each samples were normalized to 10^6 cells.

Cell TEM Observation: HeLa cells were seeded in 35 mm round tissue culture dishes and allowed to proliferate till 80% fluent. After washing twice with sterile PBS buffer, the cells were incubated with micellar nanoparticles (the concentration of Fe^{III} ions were $\approx 67.5 \times 10^{-6}$ M) for 24 h at 37 °C. The cells were washed with PBS three times in order to remove excess nanoparticles, and then were fixed by 2% glutaraldehyde in 0.1 M sodium cacodylate buffer with pH = 7.4 (SC buffer) on ice for more than 2 h. After washing three times with 0.1 M SC buffer for 5 min each, the cells were post-fixed with 1% osmium tetroxide in 0.1 M SC buffer for 1 h on ice. Then cell pellets were washed with 0.1 M SC buffer three times for 5 min, followed by a quick rinse with H_2O. The cell pellets were stained with 2% uranyl acetate (UA) for 1 h on ice. After staining, they were dehydrated in a graded series of ethanol (50%, 70%, 90%, and 100%) for 5–8 min each, and dried in acetone at room temperature. Then the cell pellets were infiltrated by 50:50 dry acetone/durcupan for 1–2 h on a rotator, followed by 100% durcupan overnight and 2X 100% durcupan next day. Finally, the cell pellets were embedded in durcupan and incubated in an oven at 60 °C for 36–48 h. Ultrathin sections were cut and were examined via electron microscopy.

NMRD Profiles Analysis: A simplified model was utilized to analyze the data and obtain an estimation for some of the relevant molecular parameters affecting the relaxivity of the system. In this model, only the high field data were considered and the fit was performed according to the Solomon–Bloembergen–Morgan (SBM) set of equations, as discussed in the main text. The determination of electron spin relaxation parameters is almost entirely dependent upon fitting the low field data. As we stated in the manuscript, low field data were not included in the fitting. The reason for this is simply that SBM theory does not function very well across this frequency range for slowly tumbling systems—a fact that has been commonly noted for many years by several different groups.[31] For this reason it would be unwise to try to attribute any genuine physical meaning to the values of Δ^2 and τ_V. We then used as adjustable parameters Δ^2, τ_V, τ_R, τ_M, and q/r^6. Satisfactory fit was obtained with the parameters reported in Table 1. The choice of $q = 2$ is arbitrary and was made since associated with the reasonable value of r of 3.3 Å. Of course, setting $q = 3$ we would obtain values for r equal to 3.72 Å. The same value was reported in the case of Fe^{III}heme-HSA.[43] A distance of 3.2 ± 0.1 Å was also reported for bovine lactoferrin.[28] The value of the rotational correlation times is much shorter than that associated with a macromolecular system and in good agreement with that expected for loosely bound second-sphere water molecules. The exchange lifetime τ_M is also very similar to that estimated for bovine lactoferrin.[28]

Supporting Information

Supporting Information is available from the Wiley Online Library or from the author.

Acknowledgements

Y.L. and Y.H. contributed equally to this work. The authors acknowledge support from the NIH (NIBIB R01EB011633), a Director's New Innovator Award (DP2OD008724), and Alfred P. Sloan Foundation to N.C.G. M.B. thanks support of the "Compagnia di San Paolo" (CSP-2012 NANOPROGLY Project).

[1] M. D. Fox, M. E. Raichle, *Nat. Rev. Neurosci.* **2007**, *8*, 700.
[2] E. Terreno, D. D. Castelli, A. Viale, S. Aime, *Chem. Rev.* **2010**, *110*, 3019.
[3] a) H. B. Na, I. C. Song, T. Hyeon, *Adv. Mater.* **2009**, *21*, 2133; b) S. Laurent, D. Forge, M. Port, A. Roch, C. Robic, L. Vander Elst, R. N. Muller, *Chem. Rev.* **2008**, *108*, 2064.
[4] R. B. Lauffer, *Chem. Rev.* **1987**, *87*, 901.
[5] a) S. Aime, P. Caravan, *J. Magn. Reson. Imaging* **2009**, *30*, 1259; b) A. Kribben, O. Witzke, U. Hillen, J. Barkhausen, A. E. Daul, R. Erbel, *J. Am. Coll. Cardiol.* **2009**, *53*, 1621.
[6] a) I. Bertini, F. Capozzi, C. Luchinat, Z. Xia, *J. Phys. Chem.* **1993**, *97*, 1134; b) I. Bertini, C. Luchinat, G. Parigi, *Adv. Inorg. Chem.* **2005**, *57*, 105.
[7] a) R. C. Hider, X. Kong, *Nat. Prod. Rep.* **2010**, *27*, 637; b) M. Auerbach, D. Coyne, H. Ballard, *Am. J. Hematol.* **2008**, *83*, 580; c) P. Yi, G. Chen, H. Zhang, F. Tian, B. Tan, J. Dai, Q. Wang, Z. Deng, *Biomaterials* **2013**, *34*, 3010; d) E. M. Shapiro, S. Skrtic, K. Sharer, J. M. Hill, C. E. Dunbar, A. P. Koretsky, *Proc. Natl. Acad.*

Sci. U.S.A. **2004**, *101*, 10901; e) M. Mahmoudi, H. Hosseinkhani, M. Hosseinkhani, S. Boutry, A. Simchi, W. Shane Journeay, K. Subramani, S. Laurent, *Chem. Rev.* **2011**, *111*, 253.

[8] D. S. Kalinowski, D. R. Richardson, *Pharmacol. Rev.* **2005**, *57*, 547.

[9] Y. Yu, E. Gutierrez, Z. Kovacevic, F. Saletta, P. Obeidy, Y. Suryo Rahmanto, D. R. Richardson, *Curr. Med. Chem.* **2012**, *19*, 2689.

[10] B. P. Lee, P. B. Messersmith, J. N. Israelachvili, J. H. Waite, *Annu. Rev. Mater. Res.* **2011**, *41*, 99.

[11] W. R. Harris, C. J. Carrano, K. N. Raymond, *J. Am. Chem. Soc.* **1979**, *101*, 2213.

[12] M. J. Harrington, A. Masic, N. Holten-Andersen, J. H. Waite, P. Fratzl, *Science* **2010**, *328*, 216.

[13] a) E. Rodríguez, R. V. Simoes, A. Roig, E. Molins, N. Nedelko, A. Ślawska-Waniewska, S. Aime, C. Arús, M. E. Cabañas, S. Cerdán, M. L. García-Martín, *Magn. Reson. Mater. Phys.* **2007**, *20*, 27; b) J. A. Davies, S. G. Dutremez, C. M. Hockensmith, R. Keck, N. Richardson, S. Selman, D. A. Smith, C. W. Ulmer, L. S. Wheatley, J. Zeiss, *Acad. Radio.* **1996**, *3*, 936; c) D. D. Schwert, N. Richardson, G. Ji, B. Radüchel, W. Ebert, P. E. Heffner, R. Keck, J. A. Davies, *J. Med. Chem.* **2005**, *48*, 7482.

[14] a) G. Ratzinger, P. Agrawal, W. Körner, J. Lonkai, H. M. Sanders, E. Terreno, M. Wirth, G. J. Strijkers, K. Nicolay, F. Gabor, *Biomaterials* **2010**, *31*, 8716; b) J. L. Turner, D. Pan, R. Plummer, Z. Chen, A. K. Whittaker, K. L. Wooley, *Adv. Funct. Mater.* **2005**, *15*, 1248.

[15] a) Y. Liu, K. Ai, L. Lu, *Chem. Rev.* **2014**, *114*, 5057; b) M. E. Lynge, R. Van Der Westen, A. Postma, B. Städler, *Nanoscale* **2011**, *3*, 4916; c) Q. Ye, F. Zhou, W. Liu, *Chem. Soc. Rev.* **2011**, *40*, 4244; d) M. d'Ischia, A. Napolitano, V. Ball, C.-T. Chen, M. J. Buehler, *Acc. Chem. Res.* **2014**, *47*, 3541; e) E. Faure, C. Falentin-Daudré, C. Jérôme, J. Lyskawa, D. Fournier, P. Woisel, C. Detrembleur, *Prog. Polym. Sci.* **2013**, *38*, 236; f) H. Lee, S. M. Dellatore, W. M. Miller, P. B. Messersmith, *Science* **2007**, *318*, 426; g) D. L. Caulder, K. N. Raymond, *Acc. Chem. Res.* **1999**, *32*, 975.

[16] a) W. S. Enochs, P. Petherick, A. Bogdanova, U. Mohr, R. Weissleder, *Radiology* **1997**, *204*, 417; b) Q. Fan, K. Cheng, X. Hu, X. Ma, R. Zhang, M. Yang, X. Lu, L. Xing, W. Huang, S. S. Gambhir, Z. Cheng, *J. Am. Chem. Soc.* **2014**, *136*, 15185.

[17] a) K.-Y. Ju, J. W. Lee, G. H. Im, S. Lee, J. Pyo, S. B. Park, J. H. Lee, J.-K. Lee, *Biomacromolecules* **2013**, *14*, 3491; b) M. Xiao, Y. Li, M. C. Allen, D. D. Deheyn, X. Yue, J. Zhao, N. C. Gianneschi, M. D. Shawkey, A. Dhinojwala, *ACS Nano* **2015**, *9*, 5454.

[18] a) T.-H. Ku, M.-P. Chien, M. P. Thompson, R. S. Sinkovits, N. H. Olson, T. S. Baker, N. C. Gianneschi, *J. Am. Chem. Soc.* **2011**, *133*, 8392; b) A. M. Rush, D. A. Nelles, A. P. Blum, S. A. Barnhill, E. T. Tatro, G. W. Yeo, N. C. Gianneschi, *J. Am. Chem. Soc.* **2014**, *136*, 7615; c) M.-P. Chien, A. M. Rush, M. P. Thompson, N. C. Gianneschi, *Angew. Chem. Int. Ed.* **2010**, *49*, 5076; d) M.-P. Chien, M. P. Thompson, C. V. Barback, T.-H. Ku, D. J. Hall, N. C. Gianneschi, *Adv. Mater.* **2013**, *25*, 3599; e) M. M. Nguyen, A. S. Carlini, M.-P. Chien, S. Sonnenberg, C. Luo, R. L. Braden, K. G. Osborn, Y. Li, N. C. Gianneschi, K. L. Christman, *Adv. Mater.* **2015**, *27*, 5547; f) Z. Wang, Y. Li, Y. Huang, M. P. Thompson, C. L. M. LeGuyader, S. Sahu, N. C. Gianneschi, *Chem. Commun.* **2015**, 51, 17108; g) C. E. Callmann, C. V. Barback, M. P. Thompson, D. J. Hall, R. F. Mattrey, N. C. Gianneschi, *Adv. Mater.* **2015**, *27*, 4611.

[19] R. Duncan, *Nat. Rev. Drug Discovery* **2003**, *2*, 347.

[20] a) Y. Geng, P. Dalhaimer, S. Cai, R. Tsai, M. Tewari, T. Minko, D. E. Discher, *Nat. Nanotechnol.* **2007**, *2*, 249; b) J. A. Champion, Y. K. Katare, S. Mitragotri, *J. Controlled Release* **2007**, *121*, 3.

[21] C. W. Bielawski, R. H. Grubbs, *Prog. Polym. Sci.* **2007**, *32*, 1.

[22] a) L. Zhang, A. Eisenberg, *J. Am. Chem. Soc.* **1996**, *118*, 3168; b) Z. Wang, Y. Li, X.-H. Dong, X. Yu, K. Guo, H. Su, K. Yue, C. Wesdemiotis, S. Z. D. Cheng, W.-B. Zhang, *Chem. Sci.* **2013**, *4*, 1345.

[23] Y. Mai, A. Eisenberg, *Chem. Soc. Rev.* **2012**, *41*, 5969.

[24] a) P. Caravan, J. J. Ellison, T. J. McMurry, R. B. Lauffer, *Chem. Rev.* **1999**, *99*, 2293; b) P. Caravan, *Chem. Soc. Rev.* **2006**, *35*, 512; c) S. Aime, M. Botta, E. Terreno, *Adv. Inorg. Chem.* **2006**, *57*, 173.

[25] a) R. B. Lauffer, W. L. Greif, D. D. Stark, A. C. Vincent, S. Saini, V. J. Wedeen, T. J. Brady, *Int. J. Rad. Appl. Instrum. B* **1988**, *15*, 47; b) M. Botta, *Eur. J. Inorg. Chem.* **2000**, 399; c) T. D. P. Stack, T. B. Karpishin, K. N. Raymond, *J. Am. Chem. Soc.* **1992**, *114*, 1512.

[26] C. Brückner, D. L. Caulder, K. N. Raymond, *Inorg. Chem.* **1998**, *37*, 6759.

[27] M. K. Kabir, M. Kawahara, H. Kumagai, K. Adachi, S. Kawata, T. Ishii, S. Kitagawa, *Polyhedron* **2001**, *20*, 1417.

[28] M. Fasano, G. Fanali, F. Polticelli, P. Ascenzi, G. Antonini, *J. Inorg. Biochem.* **2004**, *98*, 1421.

[29] S. H. Koenig, R. D. BrownIII, T. R. Lindstrom, *Biophys. J.* **1981**, *34*, 397.

[30] a) H. Xu, C. A. S. Regino, M. Bernardo, Y. Koyama, H. Kobayashi, P. L. Choyke, M. W. Brechbiel, *J. Med. Chem.* **2007**, *50*, 3185; b) J. S. Ananta, B. Godin, R. Sethi, L. Moriggi, X. Liu, R. E. Serda, R. Krishnamurthy, R. Muthupillai, R. D. Bolskar, L. Helm, M. Ferrari, L. J. Wilson, P. Decuzzi, *Nat. Nanotechnol.* **2010**, *5*, 815.

[31] P. H. Fries, E. Belorizky, *J. Chem. Phys.* **2005**, *123*, 124510.

[32] N. M. Barkey, C. Preihs, H. H. Cornnell, G. Martinez, A. Carie, J. Vagner, L. Xu, M. C. Lloyd, V. M. Lynch, V. J. Hruby, J. L. Sessler, K. N. Sill, R. J. Gillies, D. L. Morse, *J. Med. Chem.* **2013**, *56*, 6330.

[33] a) J. Yang, M. A. C. Stuart, M. Kamperman, *Chem. Soc. Rev.* **2014**, *43*, 8271; b) N. Holten-Andersen, A. Jaishankar, M. J. Harrington, D. E. Fullenkamp, G. Dimarco, L. d. He, G. H. McKinley, P. B. Messersmith, K. Y. C. Lee, *J. Mater. Chem. B* **2014**, *2*, 2467; c) N. Holten-Andersen, M. J. Harrington, H. Birkedal, B. P. Lee, P. B. Messersmith, K. Y. C. Lee, J. H. Waite, *Proc. Natl. Acad. Sci. USA* **2011**, *108*, 2651; d) H. Ejima, J. J. Richardson, K. Liang, J. P. Best, M. P. Van Koeverden, G. K. Such, J. Cui, F. Caruso, *Science* **2013**, *341*, 154.

[34] P. Caravan, *Acc. Chem. Res.* **2009**, *42*, 851.

[35] N. P. Sadler, C.-C. Chuang, R. M. Milburn, *Inorg. Chem.* **1995**, *34*, 402.

[36] a) Y. Liu, K. Ai, J. Liu, M. Deng, Y. He, L. Lu, *Adv. Mater.* **2013**, *25*, 1353; b) O. Z. Fisher, B. L. Larson, P. S. Hill, D. Graupner, M.-T. Nguyen-Kim, N. S. Kehr, L. De Cola, R. Langer, D. G. Anderson, *Adv. Mater.* **2012**, *24*, 3032.

[37] L. Tao, W. Hu, Y. Liu, G. Huang, B. D. Sumer, J. Gao, *Exp. Biol. Med.* **2011**, *236*, 20.

[38] M. Müllner, S. J. Dodds, T.-H. Nguyen, D. Senyschyn, C. J. H. Porter, B. J. Boyd, F. Caruso, *ACS Nano* **2015**, *9*, 1294.

[39] K. Zhang, R. Rossin, A. Hagooly, Z. Chen, M. J. Welch, K. L. Wooley, *J. Polym. Sci., Part A: Polym. Chem.* **2008**, *46*, 7578.

[40] A. B. Pangborn, M. A. Giardello, R. H. Grubbs, R. K. Rosen, F. J. Timmers, *Organometallics* **1996**, *15*, 1518.

[41] M. S. Sanford, J. A. Love, R. H. Grubbs, *Organometallics* **2001**, *20*, 5314.

[42] a) M. E. Hahn, L. M. Randolph, L. Adamiak, M. P. Thompson, N. C. Gianneschi, *Chem. Commun.* **2013**, *49*, 2873; b) C. F. Culberson, P. Wilder Jr., *J. Org. Chem.* **1960**, *25*, 1358.

[43] G. Fanali, G. Pariani, P. Ascenzi, M. Fasano, *FEBS J.* **2009**, *276*, 2241.

Received: September 10, 2015
Revised: October 29, 2015
Published online: December 17, 2015